Chapter 3

Plasma Flows in Cool Loops

In this chapter, we study the dynamics of low-lying cool loop systems for three data sets as observed by the Interface Region Imaging Spectrograph. Radiances, Doppler shifts, and line widths are investigated in and around observed cool loop systems using various spectral lines formed between the photosphere and transition region (TR). Footpoints of the loop threads are either dominated by blueshifts or redshifts. The cospatial variation of velocity above the blueshifted footpoints of various loop threads shows a transition from very small upflow velocities ranging from (-1 to +1) km s^{-1} in the Mg II k line (2796.20 Å formation temperature: log(T/K)=4.0) to the high upflow velocities from (-10 to -20) km s^{-1} in Si IV. Thus, the transition of the plasma flows from redshift (downflows) to blueshift (upflows) is observed above the footpoints of these loop systems in the spectral line C II (1334.53 Å log(T/K)=4.3) lying between Mg II k and Si IV (1402.77 Å log(T/K)=4.8). This flow inversion is consistently observed in all three sets of the observational data. The other footpoint of the loop system always remains redshifted, indicating downflowing plasma. The multispectral line analysis in the present chapter provides a detailed scenario of the plasma

> ***flow's inversions in cool loop systems leading to the mass transport and their formation. The impulsive energy release due to small-scale reconnection above the loop footpoint seems to be the most likely cause for sudden initiation of the plasma flows evident at TR temperatures. This work is published in "The Astrophysical Journal (ApJ)".***
>
> Yamini K. Rao, Abhishek K. Srivastava, Pradeep Kayshap, Klaus Wilhelm, and Bhola N. Dwivedi, *ApJ, 874, 1, 56 (2019)*

3.1 Introduction

Physics of the transition region (TR) of the Sun plays an important role in understanding the various dynamical plasma processes. It acts as an interface layer between the chromosphere and the lower corona. The closed magnetic structures are embedded in plasma in different regions of the Sun, e.g., quiet-Sun (QS) and active regions (ARs). The loops are anchored in the solar photosphere while their upper segments may lie either in the chromosphere and TR (low-lying loops), or in the corona. The magnetic loops are classified on the basis of their formation temperatures and emissions. There are hot loops (Dowdy, 1993), warm loops (Lenz et al., 1999) , and cool loops (Foukal, 1976) having temperatures ranging from >2 MK, (1 to 2) MK, and (0.1 to 1.0) MK, respectively. This classification also depends on the spectral regime, i.e, cool loops are visible at UV wavelengths, warm loops in extreme ultraviolet (EUV) wavelengths, and hot loops emit ultraviolet (UV), EUV, and X-ray wavelengths. But even cooler loops, possessing temperatures lower than 0.1 MK, also contribute significantly to the EUV emissions (Feldman, 1998; Sasso et al., 2012, and references cited therein) . There are different scenarios proposed for the heating of such loops, e.g., steady heating, impulsive heating, etc (Klimchuk, 2006).

The loop structures in the solar atmosphere are the manifestations of magnetic structures along which the plasma is confined. In order to understand the heating of loop plasma, thermal diagnostics have to be conducted (Landi, 2007). Though the corona sometimes flares in active regions, these loops are mostly considered to remain in a steady state (Rosner et al., 1978). This shows that the heating mechanism has to be steady enough to bring loops in an equilibrium condition. Also, the emission in coronal loops varies significantly, which is found to be more sensitive to density and less to temperature (Benz, 2008). Thus, it shows that the diagnostics of flows in coronal loops is not that simple because brightness variations can even be produced by thermal fronts and waves (Reale, 2014). Doppler shift measurements for different spectral lines along the line-of-sight direction thus provide some evidence of plasma motions. This supports mainly two types of bulk mass motions: siphon flow often observed in the cool loops due to pressure difference at different foot points or loop filling and draining, due to momentary heating and cooling, respectively. Significant downflows are driven by cooling for which two mechanisms have been proposed, namely, cool downfalling blobs of plasma or slow magnetoacoustic waves (Bradshaw & Cargill, 2005; Cargill & Bradshaw, 2013). Recently, Huang et al. (2015) have provided observational evidence of cool TR loops using Si IV (1402.77 Å) observations of the Interface Region Imaging Spectrograph (IRIS). However, very few studies have been conducted on cool loops due to instrumental limitations. Earlier, cool loops have been observed using spectral data from other instruments like the Solar Ultraviolet Measurements of Emitted Radiation (SUMER) spectrograph on the Solar and Heliospheric Observatory (SOHO) and the EUV Imaging Spectrometer (EIS) on Hinode. Doyle et al. (2006) have reported a redshift of ≈ 20 km s^{-1} in the N V (1238.82 Å) line at the footpoints of cool loops using SUMER observations. Chae et al. (2000) have presented the rotational motions along the axes of the loops having velocities of ≈ 50 km s^{-1} using H I Lyβ (1025 Å), O VI (1032 Å, 1038 Å), and C II (1037 Å) lines from SUMER in an AR. The inversion of flows from redshift to blueshift has been observed in different regions of the Sun (Brekke et al., 1997; Chae et al., 1998a; Dadashi et al., 2011; Kayshap et al., 2015;

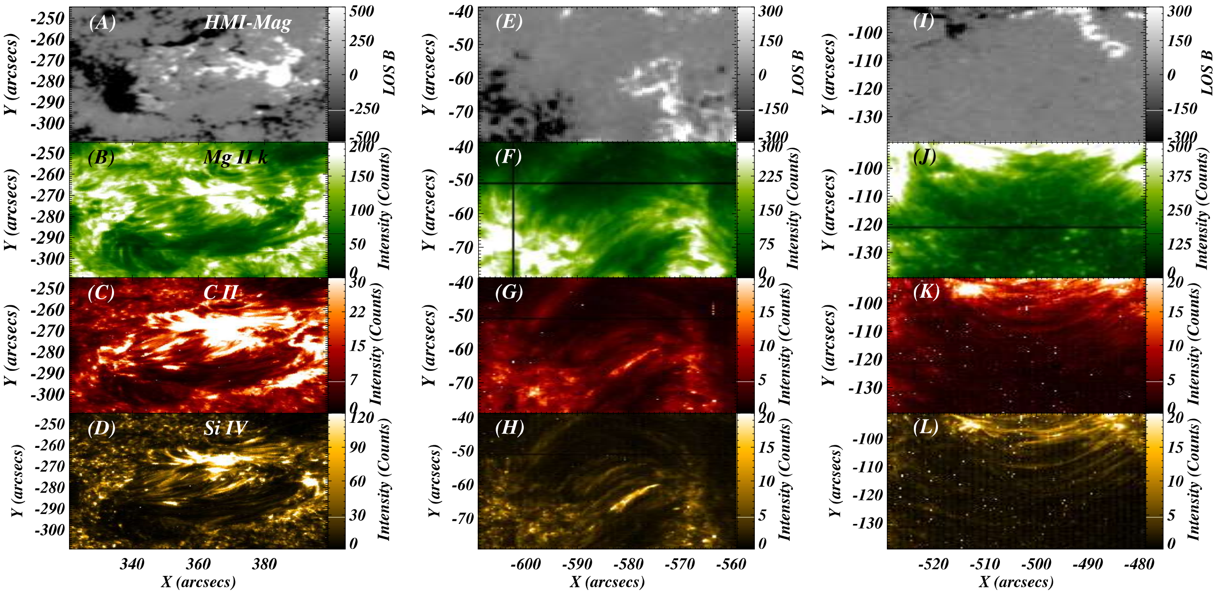

Figure 3.1: The region of interest displaying the cool loop system in different spectral lines: Mg II k (2796.20 Å), C II (1334.53 Å), and Si IV (1402.77 Å) along with the underlying magnetic polarities indicated by HMI LOS magnetogram are shown for three different datasets. The left column corresponds to Dataset 1 observed on 27th December 2013 targeting AR 11934. The middle column indicates Dataset 2 observed on 10th December 2015 targeting AR 12465. The right column shows the Dataset 3 observed on 29th March 2017 targeting AR 12645.

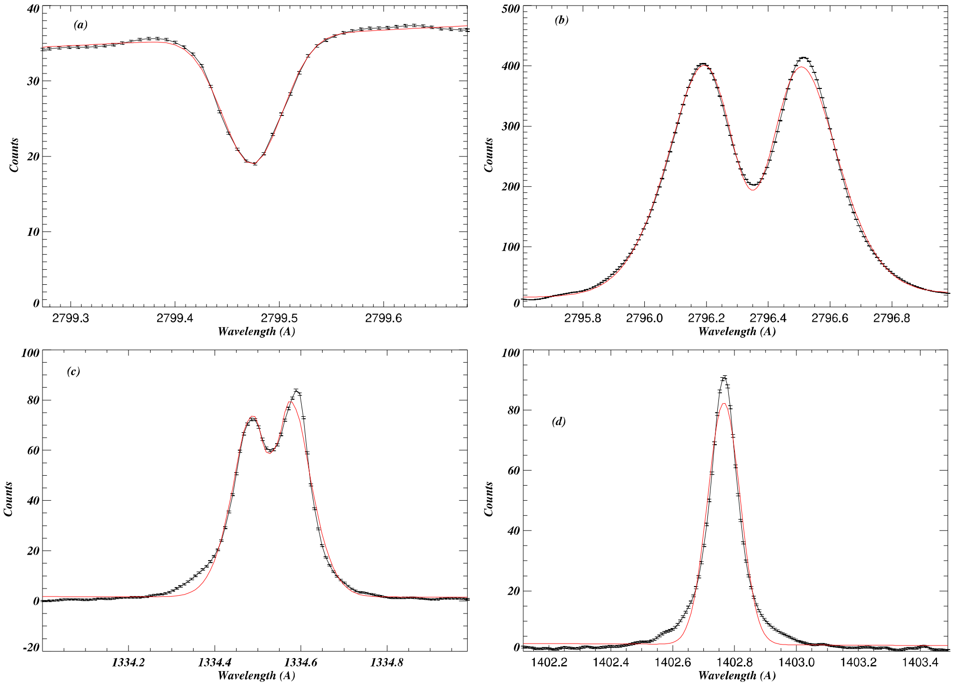

Figure 3.2: Spectral fitting of (a) Ni I (2799.47 Å), (b) Mg II k (2796.2 Å), (c) C II (1354.53 Å), and (d) Si IV (1402.77 Å) lines for averaged profile over the box labelled as B5 shown in the Si IV left panel of Fig. 3.4 corresponding to Dataset 1.

Peter & Judge, 1999; Teriaca et al., 1999; Warren et al., 1997, and references cited therein). However, flows in such cool loop systems at the chromosphere/TR interface have not been investigated in a deatiled manner.

The study of cool loops that are generally invisible at coronal temperatures, and their plasma dynamics, are important candidates to understand correctly the energy and mass transport processes in the solar atmosphere. The heights at which such flows start to propagate upward have not yet been properly understood. In order to understand the formations of cool loops, their energetics and mass supply, as well as the estimation of the flow and structure in such loops are required. Inference of plasma flows in cool loop systems, is essential to estimating flows above their footpoints at different heights using different spectral lines with different formation temperatures.

For our investigation in this work, we analyze similar regions using three different datasets comprising of cool loop systems using the spectral lines Mg II k (2796.20 Å) and Ni I (2799.47 Å) in the near ultraviolet (NUV) domain as well as in far-ultraviolet (FUV) lines C II (1334.53 Å) and Si IV (1402.77 Å) observed by IRIS (De Pontieu et al., 2014a). We study the Doppler velocity pattern above the footpoints of the cool loop systems as evident in three different spectral observational datasets. The co-spatial variation of Doppler velocities above the footpoints of the cool loop systems provides the information about regions where these plasma flows have been triggered. The other characteristic parameters such as radiance and FWHM have also been estimated to provide more insight into the response of the plasma flows in the cool loop systems. Consistency of the results is described in three different epochs of the spectral observations of cool loop systems in different parts of the Sun on different dates. In Sect. 3.2, we describe the observational data and their analyses presenting details of all the three datasets which have been used. Sect. 3.3 describes the results and their interpretation which have been classified in three different subsections of three different datasets. In each subsection, identification of loops in various spectral lines along with the magnetic polarities at their footpoints – measured with the Helioseismic and Magnetic Imager (HMI) on the Solar Dynamics Observatory (SDO) – have been discussed. The corresponding parametric maps are shown. The variation of Doppler velocity at the footpoints of the cool loop systems with different spectral lines has also been examined. In the last section, discussions and conclusions have been presented.

3.2 Observational Data and Their Analysis

Spectra from IRIS provide data in the FUV band (1331.7 Å to 1358.4 Å and 1389.0 Å to 1407.0 Å) and in the NUV (2782.7 Å to 2835.1 Å) domain having a large number of spectral lines covering the photosphere, chromosphere, TR, and inner corona. Level 2 data are used for

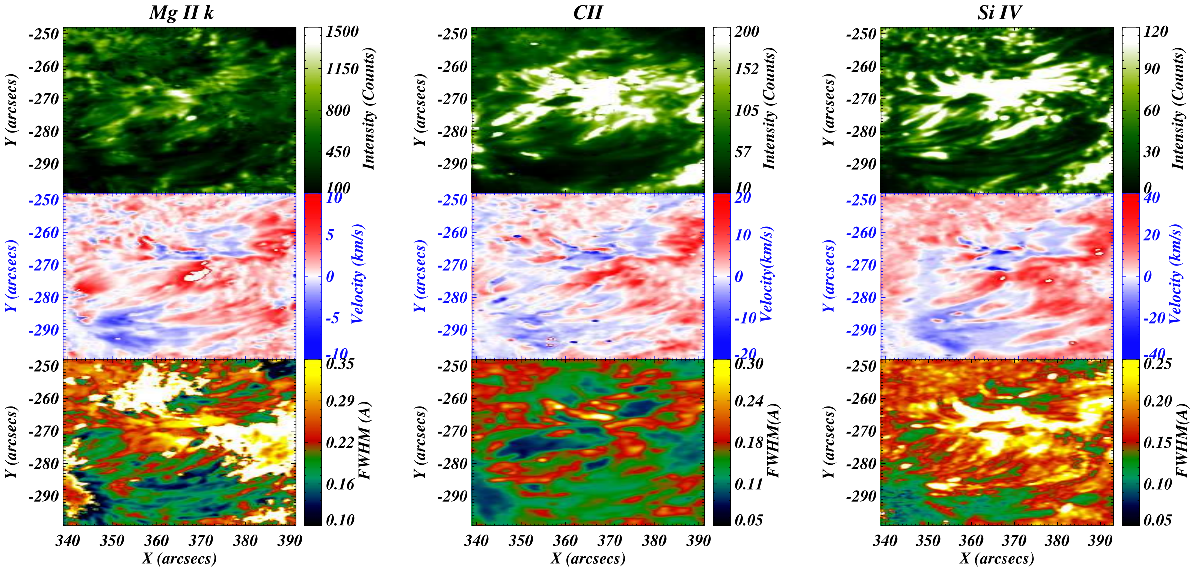

Figure 3.3: Intensity, Doppler velocity, and Full width at half maximum (FWHM) maps of Mg II k (2796.2 Å) , C II (1334.53 Å), and Si IV (1402.77 Å) lines are shown for the Dataset 1 in the left, middle, and right columns respectively.

this study, which are calibrated for the dark current removal, flat fielding. We have utilized Si IV (1402.77 Å), Mg II k (2796.20 Å), C II (1334.53 Å) and Ni I (2799.47 Å) spectral lines. We study the cool loop system for three different datasets using these spectral lines. All the datasets used for our analysis have been chosen in such a way that the loop systems should have low connectivity with magneto-plasma threads visible in SJI 1400 Å. The loop systems connected with the outer periphery of an active region or its surroundings should not contain any flare disruption. Also, the loop systems should not contain any jet activity or disruption of field lines during the whole scan of the raster, maintaining the quiet nature of the loops.

Data set 1: The data set used for our study was observed by IRIS during the time period from 22:38:08 to 23:11:59 UTC on 27th December 2013 targeting AR 11934. IRIS observed raster of 141" in the x-direction and 174" in the y-direction centred at (X_{cen},Y_{cen}) = (341", −267"). The raster scan has a temporal cadence of 5.1 s. The whole scan of the raster has 400 pixels in the x-direction with the pixel size 0.35" and 1096 pixels in the y-direction with the pixel size 0.16". The region of interest ranges from 321" to 399" in x-direction and −309" to −245" in y-direction (left-column (panel A, B, C, and D); Fig. 3.1).

Data set 2: The data set used for our study was observed by IRIS during the time period from 02:02:48 to 02:53:46 UTC on 10th December 2015 targeting AR 12465. IRIS observed raster of 112" in the x-direction and 119" in the y-direction centred at $(X_{\rm cen}, Y_{\rm cen})$ = (−615", −91"). The raster scan has a temporal cadence of 9.6 s. The whole scan of the raster has 400 pixels in the x-direction with the pixel size 0.35" and 1096 pixels in the y-direction with the pixel size 0.16". The region of interest ranges from −609" to −559" in x-direction and −79" to −39" in y-direction (middle-column (panel E, F, G, and H); Fig. 3.1).

Data set 3: The data set used for our study was observed by IRIS during the time period from from 19:59:44 to 21:00:57 UTC on 29th March 2017 targeting AR 12645. IRIS observed ranges of 141" in the x-direction and 175" in the y-direction centred at $(X_{\rm cen}, Y_{\rm cen})$ = (−517", −69"). The raster scan has a temporal cadence of 9.2 s. The whole scan of the raster has 274.50 pixels in the x-direction with the pixel size 0.35" and 200 pixels in the y-direction with the pixel size 0.35". The region of interest ranges from −529" to −479" in x-direction and −139" to −91" in y-direction (right-column (panel I, J, K, and L); Fig. 3.1).

We analyze the spectroscopic observations of various lines formed over a broad range of temperatures. We have applied iris inbuilt routine (i.e., iris_orbitvarr_corr_l2.pro) to remove the orbital variations before applying the fitting procedure. The estimation of rest wavelengths is very crucial for the estimation of Doppler velocities. We estimated the observed wavelengths of neutral lines in the very quiet area (Ni I 2799.474 Å and S I 1401.50 Å). Using the shift of the neutral lines, we have estimated the rest wavelengths of Ni I 2799.474 Å, Mg II k 2796.35 and Si IV 1402.77 Å. We estimate the observed wavelength of C II 1334.532 Å in very quiet conditions, which is used as the rest wavelength

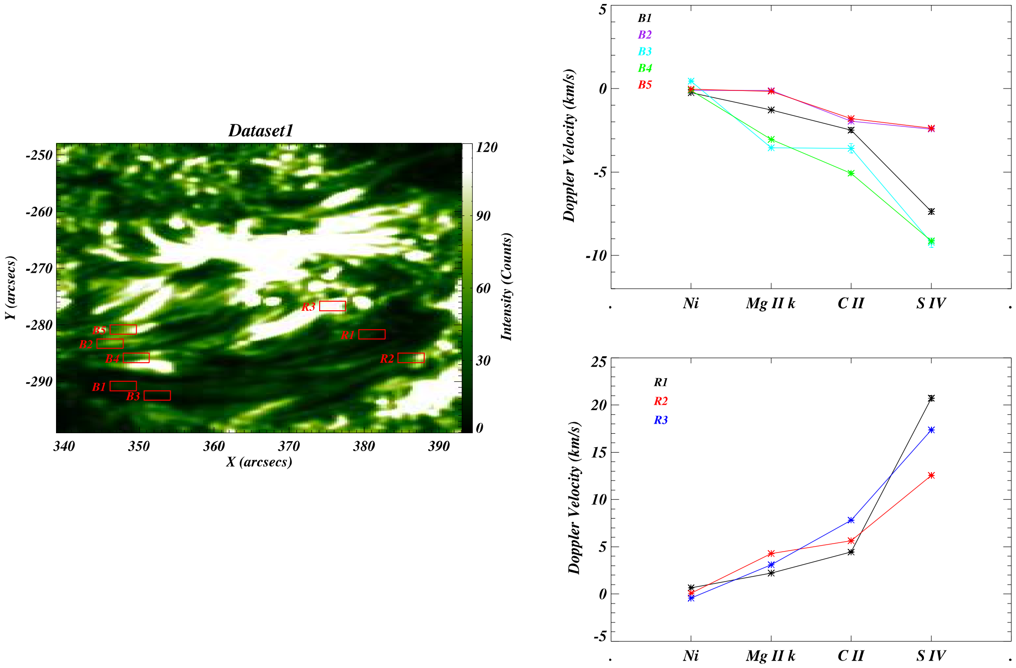

Figure 3.4: Left panel: The intensity map of Si IV (1402.77 Å) line with the boxes overlaid showing different locations at the footpoints of the cool loop systems. Top-right panel: The variation of Doppler velocity with the formation heights of different spectral lines for different boxes at the blueshifted footpoint indicated in the left panel. Bottom-right panel: The variation of Doppler velocity with the formation heights of different spectral lines for different boxes at the redshifted footpoint indicated in the left panel.

of this line. The estimated rest wavelengths of these spectral lines in each dataset are tabulated in Table 3.1. To derive the basic parameters of the line profiles, we use Gaussian fitting to lines of Ni I; formation temperature: log(T/K) = 4.2 (Stucki et al., 2000), Mg II k (2796.20 Å; log(T/K) = 4.0), C II (1334.53 Å; log(T/K) = 4.3), and Si IV (1402.77 Å; log(T/K) = 4.8) (see example fits in Fig. 3.2). The temperature coverage for different lines is indicated as provided by De Pontieu et al. (2014a). We have performed single Gaussian fitting to the Si IV line, inverse Gaussian fitting to the Ni I lines, and single or double Gaussian fitting, depending on the nature of observed profiles, to Mg II k and C II lines. Since Mg II k lines are optically thick, they provide double Gaussian profiles at most of

	Ni I (Å)	Mg II k3 (Å)	C II (Å)	Si IV (Å)
Dataset 1	2799.4745	2796.3512	1334.5391	1402.7770
Dataset 2	2799.4731	2796.3498	1334.5374	1402.7940
Dataset 3	2799.4777	2796.3544	1334.5368	1402.8001

Table 3.1: Calibrated wavelengths for different spectral line for different datasets

the locations except for sunspots (Leenaarts et al., 2013; Morrill et al., 2001; Rathore et al., 2015). The details of fitting the optically thick lines are provided in subsection 2.2.3.

3.3 Observational Results and Their Interpretation

3.3.1 Dataset 1

Identification of the cool loop system: The dynamic loop structures, which are typically visible at low temperatures of the chromosphere and TR, correspond to the cool loops. These cool loop system are present in all three datasets. The left-column of Fig. 3.1 (i.e., panel A, B, C, and D) shows the mosaic of intensity images of different spectral lines taken from the IRIS raster data along with the LOS magnetogram taken from HMI/SDO to show the cool loop system and its footpoint magnetic polarities. To create these intensity images, we have taken the averaged emission within the certain wavelengths around the central wavelengths of these lines, e.g., Mg II k (2795.0 to 2797.2) Å, C II (1334.0 to 1335.0) Å and Si IV (1402.0 to 1404) Å. This system has been taken into consideration as Dataset 1. The LOS magnetogram (Fig. 3.1; panel A) shows the presence of opposite magnetic polarities in which the foot points of the cool loop system lie. This is a multi-threaded and dynamic loop system as observed by IRIS. In the present study, we use multiple spectral lines covering wide temperature range to understand Doppler flows pattern and its variation in the observed cool loop system. The Mg II k line shows doubly peaked profiles and exhibits emission reversal for all the regions except in the sunspots (Morrill

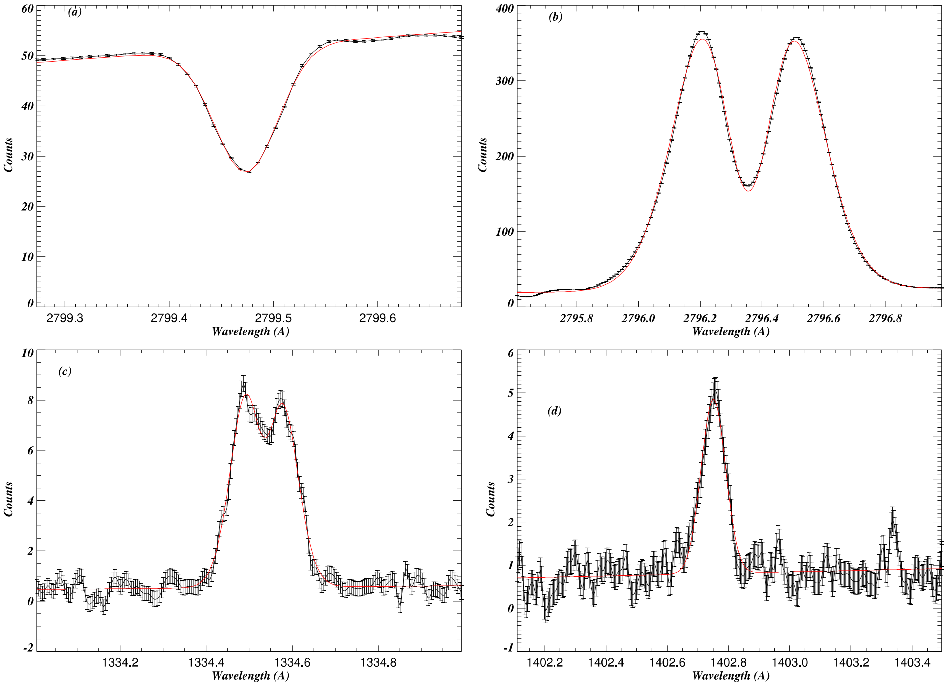

Figure 3.5: Spectral fitting of (a) Ni I (2799.47 Å), (b) Mg II k (2796.2 Å), (c) C II (1354.53 Å), and (d) Si IV (1402.77 Å) lines for averaged profile over the box labelled as B4 shown in the left panel of Fig. 3.7 corresponding to Dataset 2.

et al., 2001). The Mg II k (panel B; Fig. 3.1) and C II (Fig. 3.1; panel C) lines correspond to the chromospheric plasmas, which show the evidence of the cool loops. The top part of the loop system is not fully evident in some cool lines, however, its lower part above the footpoints are clearly visible. The loop system along with the different loop strands is clearly identified in the Si IV (Fig. 3.1; panel D) line along with its footpoint at both the ends.

Various parametric maps for the first dataset: We have selected various boxes near the footpoints of these cool loops, which are shown in the left panel of Fig. 3.4 at Si IV intensity map. Some boxes are located in blue-shifted end (e.g., B1, B2, etc) while others are located in the red-shifted end (e.g., R1, R2, etc.). These locations of the boxes are chosen to have higher emissions such that the intensity along the strand becomes more than double at the footpoint. The averaged spectra for each box is obtained by averaging all existed spectra within the particular box. Similar criteria for the selection of boxes has been followed by other datasets (Dataset 2 and Dataset 3). Fig. 3.2 presents averaged profiles of different spectral lines used in our analysis. The spectral profiles correspond to the box labelled as B5 for Dataset 1 (Fig. 3.4). The black solid line represents the averaged spectral profile for different spectral lines where corresponding errors are indicated by the error bars. The red solid line is the fitted profile on the observed profiles (black lines). We have fitted the each observed profiles within ROI to get the intensity, Dopper velocity and FWHM maps. Left column of Fig. 3.3 shows the intensity (top-left), Doppler velocity (middle-left) and FWHM maps (bottom-left) of the Mg II k. In the similar fashion, we have shown the intensity, Doppler velocity and FWHM maps of C II 1334.53 Å (middle-column) and Si IV 1402.77 Å (right-column) in Fig. 3.3. Since Mg II k is an optically thick line, it shows doubly peaked profile which has been fitted by using two Gaussians (positive and negative). Similar properties hold for the optically thick line C II 1334.53 Å. For Mg II 2796.35 Å and C II 1334.53 Å lines, we have taken the parameters from negative Gaussian, which captures the minima between two peaks. This minima basically forms in the upper chromosphere/TR. For the location exhibiting the single peak, we have taken the same parameters from positive Gaussian because only one Gaussian is present in this case. The detailed description is provided in subsection 2.2.3. Using this methodology, we have produced the intensity, Doppler velocity and FWHM maps for Mg II k and C II lines. The estimation of these maps from Si IV line is straightforward as the line is single peak line. For Mg II k, the intensity map (top-left panel; Fig. 3.3) shows the loop structures for which the footpoints are not distinct but the top part is clearly visible. Doppler velocity map (middle-left panel; Fig. 3.3) shows blue-shifted velocities at one end and red-shifted at another which has been mapped having values ranging from (-10.0 to $+10.0$) km s^{-1}.

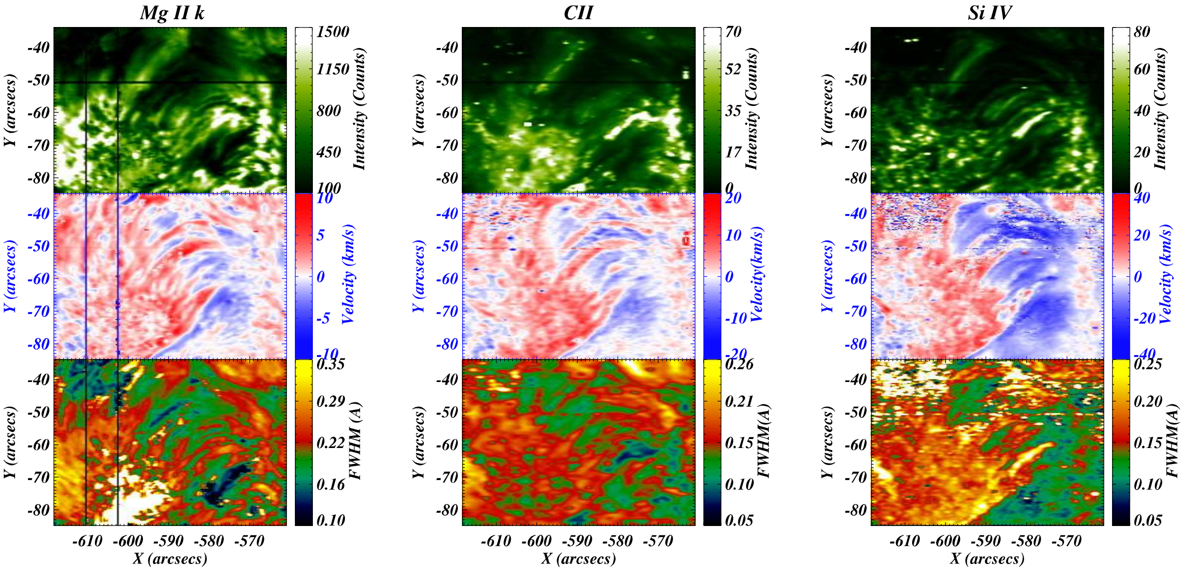

Figure 3.6: Intensity, Doppler velocity, and Full width at half maximum (FWHM) maps of Mg II k (2796.2 Å) , C II (1334.53 Å), and Si IV (1402.77 Å) lines are shown for the Dataset 2 in the left, middle, and right columns respectively.

The corresponding FWHM map is shown in the bottom-left panel of Fig. 3.3. The line width range for Mg II k varies from (0.10 to 0.35) Å.

For C II line, such parametric maps are shown in the middle-column of Fig. 3.3 where the fuzzier loops are visible (Top panel; Fig. 3.3) along with the direction of plasma flow indicated by Doppler velocity map (Middle panel; Fig. 3.3(ii)). The FWHM map of C II 1334.53 Å is displayed in bottom panel of Fig. 3.3(ii), which has values ranging from 0.05 Å to 0.30 Å. The cool loop system for Si IV line having different strands is clearly visible in the intensity image (Top panel; Fig. 3.3) representing plasma maintained at TR temperature. The corresponding Doppler velocity shows the blueshifted and redshifted opposite footpoints of the cool loop system (Middle panel; Fig. 3.3). The Si IV Doppler velocity map has also been discussed by Huang et al. (2015) targeting the same AR using Si IV line with different time duration (21:02 UT to 21:36 UTC) corresponding to different dataset. Their results are qualitatively similar to what we have observed in the Doppler velocity map of Si IV line. We have then correlated Doppler velocity maps with FWHM

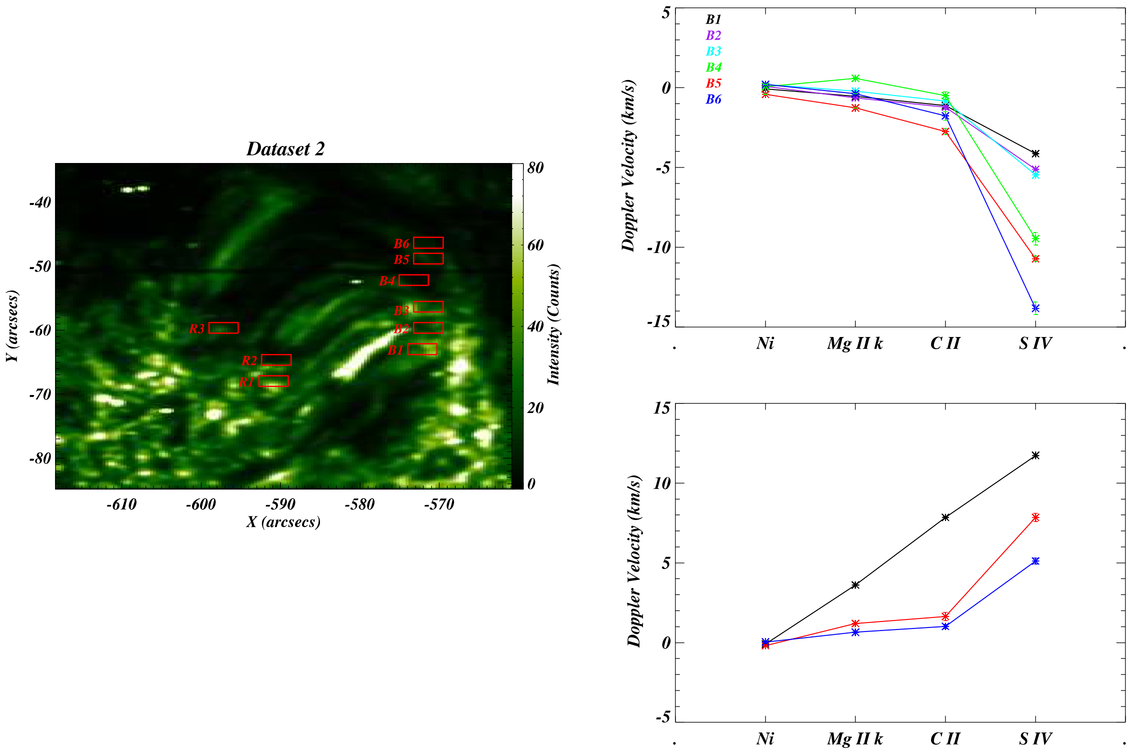

Figure 3.7: Left panel: The intensity map of Si IV (1402.77 Å) line with the boxes overlaid showing different locations at the footpoints of the cool loop systems. Top-right panel: The variation of Doppler velocity with the formation heights of different spectral lines for different boxes at the blueshifted footpoint indicated in the left panel. Bottom-right panel: The variation of Doppler velocity with the formation heights of different spectral lines for different boxes at the redshifted footpoint indicated in the left panel.

maps for Si IV line as well as some other lines which have been shown in Fig. 3.3. One end of the cool loop system is dominated by redshifts (downflows), while the other end is dominated by blueshifts (upflows). This change from blueshifts at one end to the redshifts at the other end shows the direction of plasma flows. The plasma flow structures are similar to the loop structure visible in the intensity map of the Si IV line (Top panel; Fig. 3.3). The blueshifted region shows lower values of FWHM and the redshifted end shows higher FWHM values (Bottom panels; Fig. 3.3). The corresponding values of FWHM ranging from (0.05 Å to 0.25 Å) are shown in the colorbar which exhibit the characteristics of TR.

The increased linewidth at redshifted (downflows) footpoint may be due to the heating caused by downflowing mass motions there, which are attributed to the line broadening (Tian et al., 2008, 2009).

Variation of Doppler velocity: The boxes overlaid on the intensity map of Si IV line are labelled as B1, B2, B3, B4, B5 and R1, R2, R3 (Left-panel; Fig. 3.4). These boxes indicate the locations of the footpoints of different loop strands chosen to investigate the Doppler velocities above the footpoints of the cool loop threads. The average spectral profiles from these boxes are used to infer qualitatively the Doppler velocity pattern in these regions. The photospheric signature of the footpoints of the loop system in SDO/HMI having positive and negative polarities at the opposite ends shows almost bipolar magnetic loops. Assuming the loops to have similar behaviour at the footpoints, plasma flows are investigated using Doppler velocities of multi-spectral lines. The variation of Doppler velocities is shown in the top-right panel of Fig. 3.4 corresponding to the five different boxes (i.e., B1, B2, B3, B4, and B5) at the blue-shifted footpoints of cool loop systems as shown in left panel of Fig. 3.4. The Doppler velocity of the Ni I line is very low in all boxes showing almost no upflows or downflows (-0.24 to 0.44) km s^{-1} in the photospheric region. These blueshifts (upflows) increase for B1, B3, and B4 while they remain nearly same for B2 and B5 up to the formation temperature of Mg II k. These boxes at formation temperature of Mg II k lines show considerable blue-shifts (-0.11 to -3.54) km s^{-1}. However, the significant change in the blueshifts occurs at the formation temperature of C II for the different boxes as revealed by the top-right panel of Fig. 3.4. The Doppler velocity variation at Si IV shows blueshifts having -2.42 km s^{-1} and -2.37 km s^{-1} value for B2 and B5 while the B1, B3 and B4 have high blueshifts (i.e., -7.37 km s^{-1}–B1, -9.24 km s^{-1}–B2 and -9.14 km s^{-1}–B4).

We have also considered three location labelled as R1, R2, and R3 in the redshifted region within the other footpoints of this cluster of cool loops. The Doppler velocities increase for different spectral lines showing the increase in plasma downflows as we go higher up in the solar atmosphere as shown in the bottom-right panel of Fig. 3.4. The Doppler velocity for Ni I line shows small flows having the range (−0.44 to 0.64) km s^{-1} for different locations. The optically thick lines (Mg II k and C II) are fitted as discussed in subsection 2.2.3. The centroid of the negative Gaussian is used to estimate the corresponding Doppler velocities, which range from middle chromosphere to the upper chromosphere. The Mg II k line has significant downflows having Doppler velocity range of (2.20 to 4.42) km s^{-1}. The downflows are then increased as we go higher to the formation height of C II having Doppler velocity range of (4.28 to 7.81) km s^{-1} These values reach to the maximum values of (12.53 to 20.72) km s^{-1} for Si IV line which is formed in the TR. The maximum activity is found in the upper chromosphere/TR interface where the downflows become large and create excess widths at the associated footpoints. The corresponding 1-σ error in the line centroid of the fitted profile converted into velocity terms has been shown in terms of error bars for different lines at different positions. The 1-σ velocity error being very small, it is hard to visualize these errors in the corresponding figures (see Fig. 3.4).

Line widths of Si IV at red- and blueshifted footpoints of cool loops: We have also investigated the FWHM of the Si IV line within all boxes (blue as well as red) for the first data set. The FWHMs of the blue boxes of the first observation is 0.095 Å (B1), 0.127 Å (B2), 0.114 Å (B3), 0.153 Å (B4), and 0.123 Å (B5), while the red boxes have widths of 0.215 Å (R1), 0.185 Å (R2), and 0.246 Å (R3).

Thermal width (σ_{th}) of Si IV line is 0.09 Å while the instrumental width (σ_{inst}) is 0.026 Å (De Pontieu et al., 2014a). Therefore, the non-thermal component of the line-widths (σ_{nt} = $({\sigma_{obs}}^2 - {\sigma_{th}}^2 - {\sigma_{inst}}^2)^{1/2}$) derived by the averaged spectral line profiles at different blueshifted boxes (B1 - B5) range between 0.015 Å and 0.120 Å. The plasma upflow is also associated with these regions of increased non-thermal width. In the present observational baseline, we conjecture the presence of localized energy release due to small-scale magnetic reconnection above the footpoints of the cool loop threads, and filling-up of the evaporated plasma in these threads which we observe in form of the blueshift (e.g., Hansteen et al., 2014; Huang et al., 2015; Patsourakos & Klimchuk, 2006; Polito et al., 2015).

It is obvious that the redshifted footpoints have higher line widths (almost double) compared to the blueshifted footpoints. The downfall or condensation of the cool-loop plasma towards their redshifted foot-points in TR may contribute into the line width broadening (Tian et al., 2009). There may be additional physical processes which may cause excess line broadening on the red-shifted TR footpoints of the loop system, *viz.*, nano-flare generated acoustic waves (Hansteen, 1993) from the overlying atmosphere, overall downward propagating pressure disturbances (Zacharias et al., 2018), etc.

3.3.2 Dataset 2

Identification of cool loops: The middle-column of Fig. 3.1 shows the region of interest consisting of cool loop system for Dataset 2 along with the magnetic polarities at the footpoints shown by LOS magnetogram (Fig. 3.1; panel E). The observational signatures of the existence of cool loop system are shown using Mg II k (Fig. 3.1; panel F), C II (Fig. 3.1; panel G) and Si IV (Fig. 3.1; panel H) lines intensity maps. The intensity map of Si IV line (Fig. 3.1; panel H) shows faint loops corresponding to the temperatures of the transition region. The characteristic behaviour of the loop system for different spectral lines is similar to that of description for Dataset 1 (left-column; Fig. 3.1).

Parametric maps for the second dataset: Fig. 3.5 represents average observed profiles (averaged over the selected boxes B4) of different spectral lines. The displayed spectral profiles correspond to the box labelled as B4 for Dataset 2 (Left- panel; Fig. 3.7). Fig. 3.6 shows the intensity, Doppler velocity, and FWHM maps for Mg II k (Fig. 3.6; left-column), C II (Fig. 3.6; middle column), and Si IV (Fig. 3.6; right-column). The Doppler

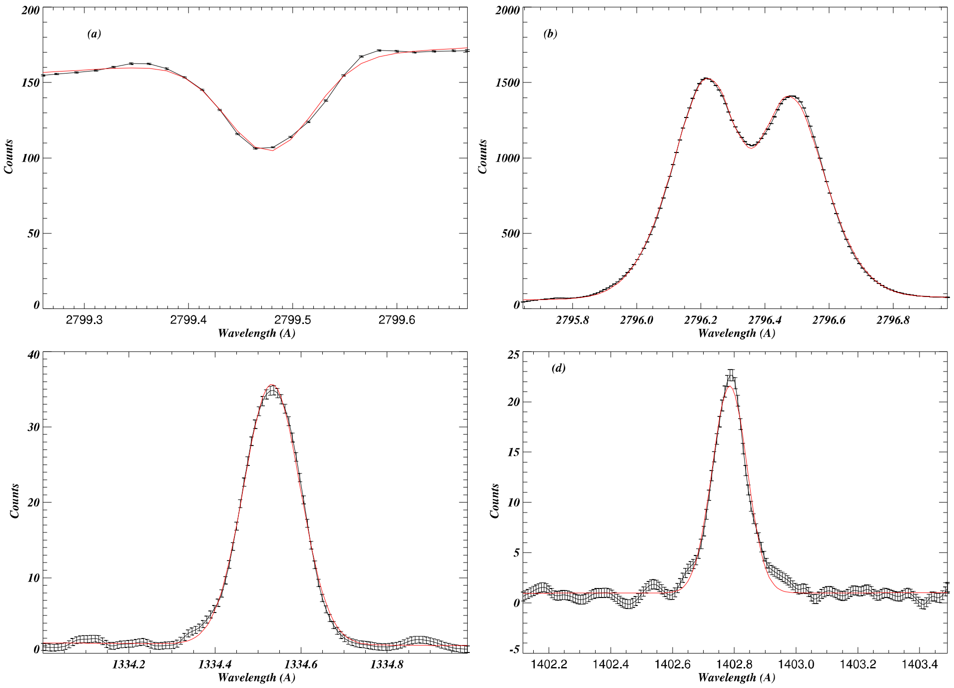

Figure 3.8: Spectral fitting of (a) Ni I (2799.47 Å), (b) Mg II k (2796.2 Å), (c) C II (1354.53 Å), and (d) Si IV (1402.77 Å) lines for box labelled as B3 in the left panel Fig. 3.10 for Dataset 3.

velocity maps (middle-panel in each column; Fig. 3.6) show that one of the footpoint is red-shifted while the other is blueshifted. The upflowing plasma (i.e., the blueshifted end) is falling to the other end, which causes redshifts there. The corresponding values of Doppler velocity are shown by the colorbars in each panel. The line widths are represented by FWHM maps in the bottom panels of Fig. 3.6 for Mg II k3 (left-cloumn), Fig. 3.6 for C II (middle-column), and Fig. 3.6 for Si IV (right-column) where the increased linewidth at the redshifted footpoint might be due to downflowing plasma (Tian et al., 2008, 2009).

Variation of Doppler velocity: The locations used for Doppler velocity estimations are labelled as B1, B2, B3, B4, B5, B6 and R1, R2, R3 at the blue-shifted and red-shifted footpoints of the cool loop system for Dataset 2 shown in the left panel of of Fig. 3.7. The top-right panel shows the variation of Doppler velocity for Dataset 2 at the blueshifted footpoints of the cool loop system for boxes shown in left panel of Fig. 3.7.

The Doppler velocity of the Ni I line is very low in all boxes showing almost no upflows or downflows (-0.07 to 0.44) km s^{-1} in the photospheric region. These flows show small redshifts/blueshifts for selected different boxes at the formation temperature of Mg II k. All these flows show considerable blue-shifts (-0.50 to -2.74) km s^{-1} at C II. The Doppler velocity at Si IV shows high blueshifts for B4, B5, and B6 having maximum value of -13.83 km s^{-1}. However, the boxes B1, B2, and B3 show relatively small upflows having velocity (-4.13 to -5.47) km s^{-1}. The corresponding error bars (1-σ error) are overplotted; however, they are not visible due to their very small amplitudes.

We have also considered three locations within the the redshifted footpoints of this cluster of cool loops, which are labelled as R1, R2, and R3. The Doppler velocities increase for different spectral lines showing the increase in plasma downflows as we go higher up in the solar atmosphere as shown in the bottom-right panel of Fig. 3.7. The Doppler velocity for Ni I line shows small flows having range (-0.08 to 0.04) km s^{-1}. The Mg II k line has relatively small downflows having Doppler velocity range of (0.65 to 3.61) km s^{-1}. The downflows are then increased as we go higher to the formation height of C II having Doppler velocity range of (1.01 to 7.84) km s^{-1}. These values reach maximum values of (5.11 to 11.73) km s^{-1} for Si IV line. The maximum activity is found in the upper chromosphere/TR interface, where the downflows become large and create excess widths at the associated footpoints.

Line widths of Si IV at red and blue-shifted footpoints of cool loops: We have also investigated the FWHM of the Si IV line within all boxes (blue as well as red) for the second data set. FWHM of the blue boxes of second observation is 0.107 Å (B1), 0.105 Å (B2), 0.108 Å (B3), 0.094 Å (B4), and 0.131 Å (B5), and 0.141 Å (B6). While, the red boxes have widths of 0.200 Å (R1), 0.186 Å R2), and 0.187 Å (R3) indicating higher line-widths at the red-shifted locations. A similar trend of FWHM in blue and red boxes is

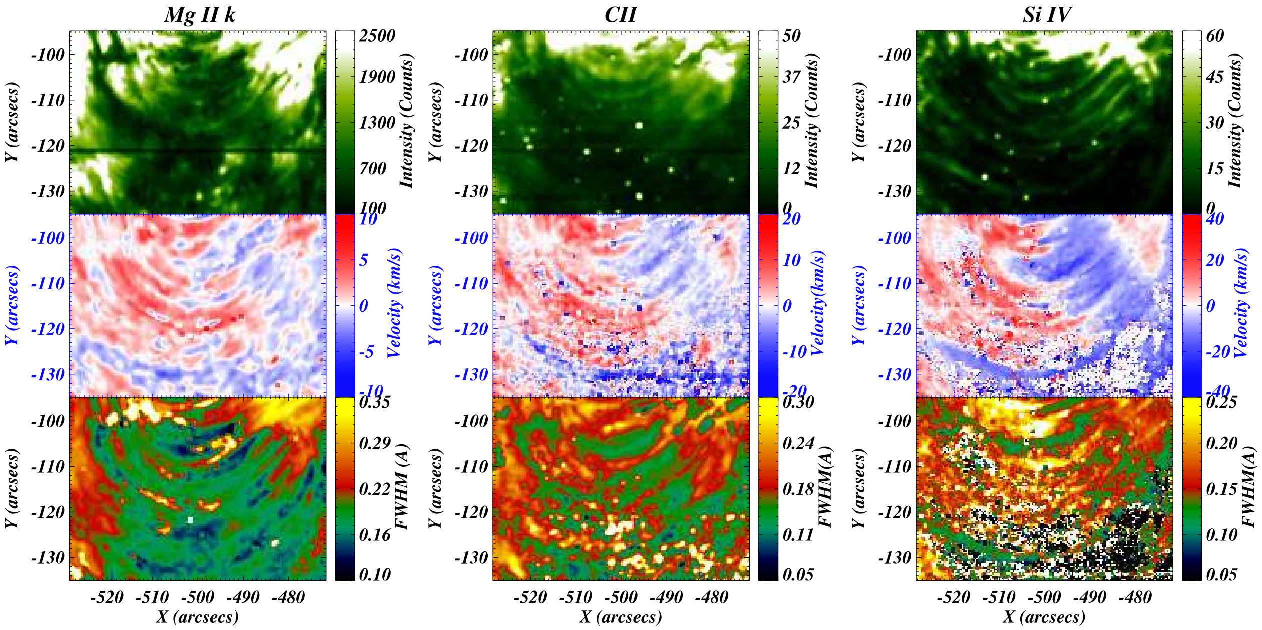

Figure 3.9: Intensity, Doppler velocity, and Full width at half maximum (FWHM) maps of Mg II k (2796.2 Å) , C II (1334.53 Å), and Si IV (1402.77 Å) lines are shown for the Dataset 3 in the left, middle, and right columns respectively.

also found in this observation as Dataset 1; therefore, the possible physical implications remain same.

3.3.3 Dataset 3

Identification of cool loops: The right column of Fig. 3.1 shows the mosaic of the intensity images for different spectral lines for Dataset 3 along with the magnetic polarities at the footpoints shown by LOS magnetogram (Fig. 3.1; panel I). The loop strands are visible as clearly resolved structures in Si IV line intensity (Fig. 3.1; panel L) while Mg II k (Fig. 3.1; panel J) and C II (Fig. 3.1; panel K) shows chromospheric/TR signatures and the loop strands appear fuzzier. The loop structures are thus shown at different wavelengths corresponding to different formation heights in the solar atmosphere. The LOS magnetogram indicates the opposite magnetic polarities at the footpoints of the cool loop system.

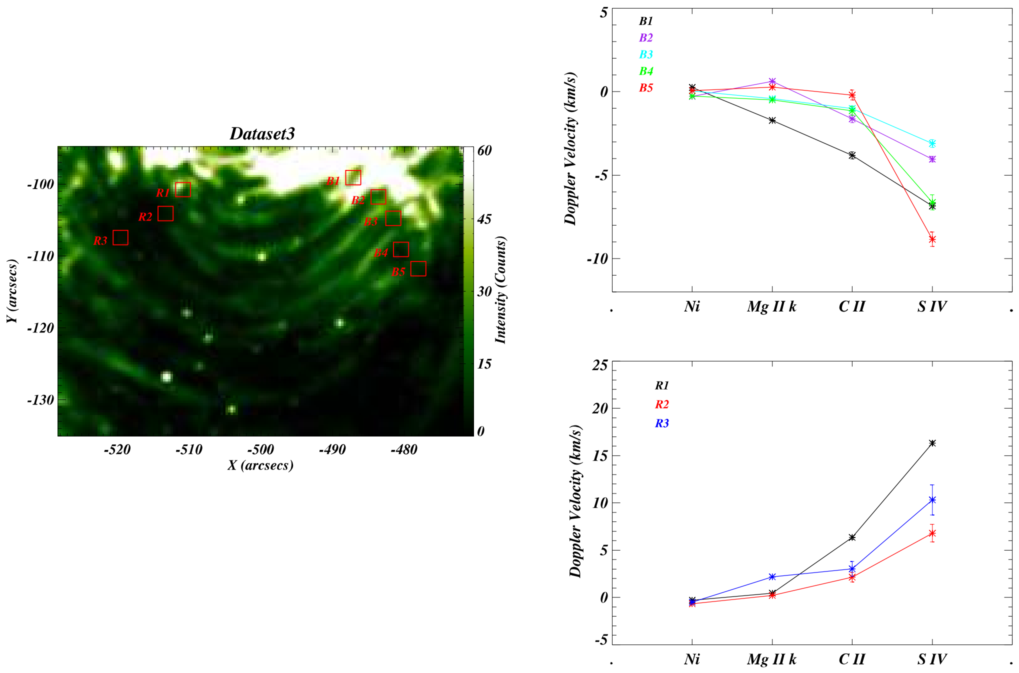

Figure 3.10: Left panel: The intensity map of Si IV (1402.77 Å) line with the boxes overlaid showing different locations at the footpoints of the cool loop systems. Top-right panel: The variation of Doppler velocity with the formation heights of different spectral lines for different boxes at the blueshifted footpoint indicated in the left panel. Bottom-right panel: The variation of Doppler velocity with the formation heights of different spectral lines for different boxes at the redshifted footpoint indicated in the left panel.

Parametric maps for the third dataset: Fig. 3.8 represents average profiles of different spectral lines correspond to the box labelled as B3 for Dataset 3 (Left-panel; Fig. 3.10). Fig. 3.9 shows the intensity, Doppler velocity, and FWHM maps for Mg II k (Fig. 3.9; left-column), C II (Fig. 3.9; middle-column), and Si IV line (Fig. 3.9; right-column). The plasma emissions in the intensity maps (Top-panels; Fig. 3.9) are similar to the direction of plasma flows in the Doppler velocity maps (Middle-panels; Fig. 3.9) having blueshifts at one end and redshifts at the other end. The linewidths in the bottom panels of Fig. 3.9 show the mass motions signatures of the plasma having high values of FWHM at the redshifted footpoint indicating the heating caused by downfalling plasma (Tian et al., 2008, 2009).

Variation of Doppler velocity: In Fig. 3.10, the top right panel shows the variation of Doppler velocity for Dataset 3 at the blueshifted footpoints of the cool loop system for boxes shown in Fig. 3.9. The Doppler velocity of the Ni I line is very low in all boxes showing almost no upflows or downflows (-0.05 to -0.28) km s^{-1} in the photospheric region. These flows show small redshifts and blueshifts for different boxes at the formation temperature of Mg II k lying in the range (-1.72 to 0.61) km s^{-1}. Interestingly, all these boxes show considerable blueshifts (-0.19 to -3.81) km s^{-1} at C II. The Doppler velocity variation at Si IV shows high blueshifts for having maximum value of -8.84 km s^{-1} for B5.

In the similar fashion as we did in the previous cases, we have also considered three boxes in the redshifted region near other footpoints of this cluster of cool loops. The redshifts increase for different spectral lines showing the increase in plasma downflows as we go higher up in the solar atmosphere as shown in the bottom-right panel of Fig. 3.10. The maximum activity is found in the upper chromosphere/TR interface where the downflows become large and create excess widths at the associated footpoints. The variation of Doppler velocities above redshifted footpoint for different boxes (R1, R2, and R3) shows the increasing trend as observed in previous datasets for downflowing velocities at different formation heights of the spectral lines where the maximum values reaches the formation height of Si IV having Doppler velocity range (6.79 to 16.31) km s^{-1}.

Line widths of Si IV at red and blue-shifted footpoints of cool loops: We have also investigated the FWHM of the Si IV line within all boxes (blue as well as red) for the third data set. The FWHM of the blue boxes of third observation is 0.149 Å (B1), 0.135 Å (B2), 0.134 Å (B3), 0.125 Å (B4), and 0.126 Å (B5), while the red boxes have the widths of 0.182 Å (R1), 0.139 Å (R2), and 0.172 Å (R3). Possible physical explanations for such excess width have already been mentioned for the Datasets 1 and 2.

3.4 Discussion and Conclusions

We have studied various cool loop systems in order to understand the co-spatial variations of Doppler velocities at various locations with blueshifted footpoints as well as redshifted footpoints for different spectral lines having different formation heights. The Doppler variation shows the increasing height trend in the solar atmosphere.

The photospheric, as well as chromospheric, regions show very small blueshifts of $\sim(+1 \text{ to } -1)$ km s^{-1}, which exhibit almost no upflow signatures until Mg II k. On the contrary, the C II lines are significantly blueshifted by $\sim(-1 \text{ to } -6)$ km s^{-1}. The blueshifted nature becomes more prominent at the formation temperature of Si IV. In Dataset 1 and Dataset 2, upflows are indicated above C II formation height at the blueshifted footpoints, which is well supported by the downflowing plasma at the redshifted footpoints. However, for the Dataset 3, these upflows start below C II formation height (upper chromosphere) and then driven by plasma inertia to higher heights until Si IV, and shows small downflows at C II at redshifted footpoints. All the blueshifted locations for the same dataset follow similar pattern but have different ranges of Doppler velocities showing the localised impulsive events. These flows are initiated by short impulsive events that are highly localised in the upper chromosphere or lower TR. Such localised impulsive events above or below the C II formation height make the loops thermally unstable.

Thus, the significant plasma upflows take place between the formation heights of C II and Si IV lines for Dataset 1 and Dataset 2, while it takes place below the formation heights of C II. The transition of small upflow to high upflow velocities takes place near the formation height of C II line, which justifies the origin site of plasma flow in these cool loops.

Different plausible mechanisms have been already discussed for the origin of flows in coronal loops, e.g., siphon flow (Hood & Priest, 1981), downward propagating acoustic waves (Hansteen, 1993), explosion below corona (Teriaca et al., 1999), acoustic waves

(Taroyan et al., 2005) and nanoflare driven chromospheric evaporation (Patsourakos & Klimchuk, 2006). However, the occurence of implusive heating involving magnetic reconnection has recently been reported in support of the plasma flows in the cool loop systems (Huang et al., 2015).

Warren et al. (2002) have suggested the impulsive heating of active region hot loops using TRACE observations. Spadaro et al. (2003) have also explained the flows in the coronal loops due to transient heating near the chromsophere. The outflow locations at the footpoints in cool loop systems have higher emissions indicating the dynamical nature of the loops. Localised impulsive energy release might be driving such flows since there are no flows at a few footpoints of the cool loop system (B1, B2, B3; Fig. 3.7) while other footpoints near it show upflows. The heating due to impulsive energy release gets deposited at that footpoint to drive the upflows. That portion of the flowing plasma arriving at the opposite footpoint, causes an enhancement of the linewidth. Thus, the speculation of such loop systems driven by heating pulses due to magnetic reconnection is supported by our observations. The non-thermal broadening of Si IV line at the blueshifted footpoints of the cool loop system is most likely associated with the ongoing transient energy release and thereafter filling-up of the plasma in loop threads (e.g., Hansteen et al., 2014; Huang et al., 2015; Patsourakos & Klimchuk, 2006; Polito et al., 2015). Redshifted footpoints in the Si IV line indicates that the TR plasma is flowing down on the other end of the loop system, and the excess non-thermal width may be associated with the variety of physical processes there, e.g., downfalling of the plasma (Tian et al., 2009), nano-flare generated acoustic waves (Hansteen, 1993), downward propagating pressure disturbances (Zacharias et al., 2018), etc. The exact answer is still an open question what physical process(es) causes these TR footpoints of the cool loop threads with excess line-width.

Since the transition of plasma upflows start at the TR (near the C II line formation height), they can transport mass and energy directly to the inner corona above the cool loop systems. Therefore, such loop systems play a significant role in the mass, energy, and momentum transport. They may be the lower counterparts of high temperature coronal loops. High speed plasma flows in the magnetic domain of the loops have been observed in the solar atmosphere (Harra et al., 2008). However, there are several unclear propositions regarding the origin of such fast flows. The possible transport of the plasma from the low-lying cool loop systems (the one we observed) to the higher magnetic field configuration where the plasma acceleration starts, may be the most likely source. Such plasma flows, after their acceleration in the higher atmosphere, may provide the plasma for the solar wind, if the open field lines exist in the vicinity of the footpoints of such loops; though, such an has not been observed in our case.

In conclusion, our work emphasizes the significance of plasma flows at different formation heights of the spectral lines corresponding to different regions of the solar atmosphere in a cool loop system. The height-dependent trend of the Doppler velocities explores the region where these flows start to show prominent upflows. Such flows do not start from the photosphere. On the contrary, they start from the upper chromosphere and TR where transition from small blueshifts to significantly high blueshifts have been identified in such a system. Future investigations would be required for comparing the Doppler velocity patterns in cool and hot coronal loops using multi-line spectroscopy in order to differentiate the underlying causes and different origins of the plasma flows there. In the next chapter 4, we demonstrate the modelling of the origin of plasma flows in the cool loop system.